Research Article | Vol. 27, No. 26 / 23 December 2019 / Optics Express 37224
Optics EXPRESS

Channel-closing effects of electronic excitation in solids

JIAPENG LI,[1] LIANG LI,[1] QINGBIN ZHANG,[1,3] XIAOSONG ZHU,[1] TENGFEI HUANG,[1] PENGFEI LAN,[1,4] AND PEIXIANG LU[1,2]

[1]*Wuhan National Laboratory for Optoelectronics and School of Physics, Huazhong University of Science and Technology, Wuhan 430074, China*
[2]*Hubei Key Laboratory of Optical information and Pattern Recognition, Wuhan Institute of Technology, Wuhan 430205, China*
[3]*zhangqingbin@hust.edu.cn*
[4]*pengfeilan@mail.hust.edu.cn*

Abstract: We investigate the electronic excitation of solids in strong fields by solving the time-dependent Schrödinger equation. The excitation probability exhibits a strong modulation as a function of laser intensity when the initial states fill in the whole valence band. To have a clear insight into the modulation, we further study the electronic excitation from a single eigenstate in solids. A series of resonance-like enhancements of excitation probability are produced by changing the laser intensity and wavelength. We attribute the resonance-like enhancements to the channel-closing effects in solids. It is shown that the excitation probability exhibits enhancements when the value of channel is odd for intracycle interference and an integer for intercycle interference. This is different from the atom that the enhancement occur in the integer channels. We also reveal that the channel-closing effects can be observed by solid high-order harmonic generation.

1. Introduction

With the rapid development of laser technology, numerous interesting strong-field phenomena have been observed [1–5]. Above-threshold ionization (ATI) and high-order harmonic generation (HHG) in the atom as the prominent processes among these phenomena have been extensively studied over the past decades [6–18]. A very intriguing feature of ATI or HHG lies in the dependence of these phenomena on the intensity of the laser field [19–22]. The photoelectron or high-order harmonic present resonance-like enhancements as a function of the laser intensity, such that an alteration of a few percent in the field strength may enhance the spectral intensity by an order of magnitude. Previous investigations [23–25] show that the resonance-like enhancements are attributed to the closing of a multiphoton ionization channel in a laser field. The ionization peaks when

$$R = \frac{I_p + U_p}{\hbar\omega} \tag{1}$$

is interger, where R indicates the number of photons absorbed by the atom and is called the channel-closing number. I_p is the ionization potential of the target atom, and $U_p = F_0^2/4\omega^2$ is the ponderomotive energy. F_0 and ω are the amplitude and angular frequency of the laser field, respectively. The enhancements merely appear in a portion of the ATI spectra (located at $6U_p$ and $8U_p$) and the harmonic spectra [25]. For ATI, the low-energy part of the spectrum and the part preceding the cutoff depend much more smoothly on the intensity.

Compared with the atom, the solids exhibit unique optical and electronical properties with periodic structure and high density. Recently, the study of strong-field electronic dynamics in bulk solids has attracted extensive attention [26–42] due to its potential impact on future technologies such as emerging petahertz electronic signal processing [43,44] or strong-field optoelectronics

#378925 https://doi.org/10.1364/OE.27.037224
Journal © 2019 Received 26 Sep 2019; revised 7 Nov 2019; accepted 19 Nov 2019; published 9 Dec 2019

Optics EXPRESS

[45,46]. Excitation probability induced by a laser field as a crucial step plays a fundamental role in electronic dynamics in solids. It is important to understand the underlying mechanism of the electronic excitation.

In this work, the electronic excitation from valence band (VB) to conduction bands (CBs) in strong fields is investigated by solving the time-dependent Schrödinger equation. The excitation probability is maximized at specific intensity when the initial state fills in the whole VB. We further study the electronic excitation in solids from a single eigenstate. A series of resonance-like enhancements of excitation probability are produced with specific laser intensities and wavelengths. We attribute the resonance-like enhancements to the channel-closing effects in solids. However, different from the atom, the enhancements occur when the value of channel is odd for intracycle interference and an integer for intercycle interference. The resonance-like enhancements of excitation probability also exist in other eigenstates. We also propose a scheme to observe the channel-closing effects using solid HHG.

2. Theoretical model

2.1. Electronic excitation in solids

To investigate the electronic excitation in solids, we numerically solve the time-dependent Schrödinger equation (TDSE) based on a one-dimensional periodic structure. In the length gauge with the dipole approximation, the time-dependence Hamiltonian is written as

$$\hat{H}(t) = \hat{H}_0 + xF(t), \tag{2}$$

where $\hat{H}_0 = \hat{p}^2/2 + v(x)$ is the field-free Hamiltonian and $F(t)$ is the electric field. $v(x)$ is the periodic potential of the lattice. Atomic units are used unless stated otherwise. Herein, we use the Mathieu-type potential $v(x) = -v_0[1 + \cos(2\pi x/a_0)]$ to describe the lattice potential of solids, with $v_0 = 0.37$ a.u. and lattice constant $a_0 = 8$ a.u. The parameters are chosen to mimic the structure of a semiconductor with wide band gap [47–50], such as the Zincblende AlN. The Mathieu-type potential [51] has been widely used in optical lattice research area [52,53] and strong-field electronic dynamics in solids [54–59]. We perform all calculations in the coordinate space within the region $[-396, 396]$ a.u. (99 lattice periods). To overcome the unphysical reflections of the wave function at the edges of the grid, an absorbing boundary $g(x)$ is used and it is given by

$$g(x) = \begin{cases} 1 & |x| \le \frac{L_0}{2} - R_x \\ \cos^{\frac{1}{6}}\left(\frac{\pi(|x| - \frac{L_0}{2} + R_x)}{2R_x}\right) & |x| > \frac{L_0}{2} - R_x. \end{cases} \tag{3}$$

$R_x = 66$ a.u. is the width of the absorbing boundary. $L_0 = 792$ a.u. is the width of the coordinate space. Following the method used in previous works [54,59], the expression of the dipole moment operator $xF(t)$ is the same in the entire coordinate space.

In the absence of an external laser field, the eigenvalue equation of the field-free Hamiltonian $\hat{H}_0$ is written as

$$\hat{H}_0\varphi_n(x) = E_n\varphi_n(x), \tag{4}$$

where n is the eigenvalue number and $\varphi_n(x)$ is the corresponding eigenstate. The energy bands can be obtained by solving the eigenvalues and eigenstates of $\hat{H}_0$ on the coordinate grid. The obtained band structure calculated with the diagonalization scheme is shown in Fig. 1(a). The VB and the first conduction band (CB1) can be clearly distinguished. The eigenstate numbers $100 - 198$, $199 - 297$ correspond to VB and CB1, respectively. The energy gap between VB and CB1 is $E_g = 4.2$ eV. The other bands are also calculated but not shown here. We also calculate the band structure by using the Bloch-state basis [56,57]. The obtained band structure is shown in Fig. 1(b). Comparing the energy bands in Figs. 1(a) and 1(b), one can see that the number

Optics EXPRESS

of bands, the width of the bands and the band gaps obtained by the two methods are in good agreement. This confirms the accuracy of our calculated field-free energy bands.

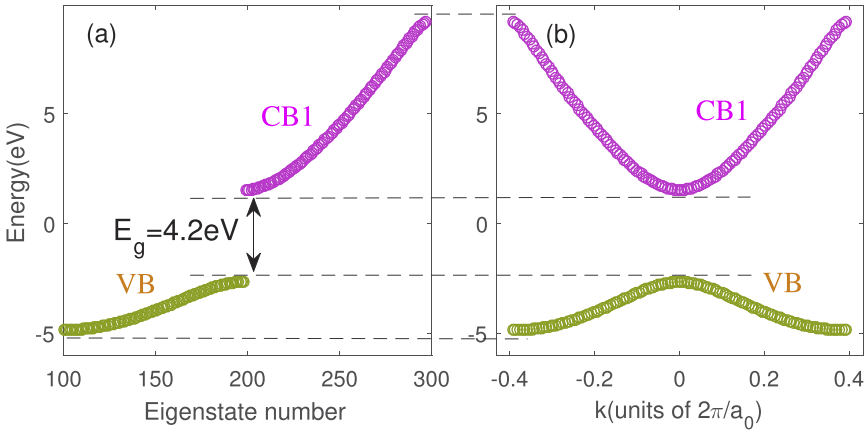

Fig. 1. (a) The band structure calculated by the diagonalization scheme in coordinate space. (b) The band structure calculated by Bloch-state expansion in reciprocal space. Only two bands are shown.

With the single-active electron approximation, the motions of electron of different eigenstates can be solved separately. The evolution of the time-dependent wave function $\psi(t)$ can be obtained by numerically solving the TDSE with the second-order split-operator method [60]. In order to make the electric field have the same form in every cycle, the laser pulse is described by $F_0 \cos(\omega t)$, where F_0 is the amplitude. The total duration of this laser pulse is four optical cycles. We also perform the electric field with a trapezoidal envelope to simulate excitation probability. The total durations is six and ten cycles, respectively. Comparing the excitation probability calculated with and without the envelope, they have the same resonant features.

After the laser pulse is gone, a fractional electrons survive at CBs. The population of the electrons remaining on CBs is called real population [44]. To obtain the real population, we project the wave function onto the eigenstates on CBs

$$|C_n|^2 = |\langle \varphi_n \mid \psi_{end} \rangle|^2 . \tag{5}$$

where ψ_{end} is the wave function at the end of the TDSE evolution. Then the real population are calculated by $\sum_n |C_n|^2$, which correspond to the excitation probability. Note that the electrons are mainly excited to CB1 in our condition.

The movement of electrons in the laser field produces a current. The laser-induced current $j(t)$ can be obtained from the time-dependent wave function:

$$j(t) = -\langle \psi(t) | \hat{p} | \psi(t) \rangle . \tag{6}$$

The harmonic spectrum is obtained from the Fourier transform of the laser-induced current:

$$H(w) \propto \left| \int j(t) e^{iwt} dt \right|^2 . \tag{7}$$

2.2. Ionization in the atom

We numerically solve TDSE in length gauge to obtain the ionization in the atom. The one-dimensional model potential of the atom is given by

$$V(x') = -\frac{1}{\sqrt{(x'^2 + a)}}, \tag{8}$$

Optics EXPRESS

where $a = 0.7242$ to obtain the ionization potential that close to helium $I_p = 0.9043$. The ground state wave function is obtained using imaginary time propagation method. We perform the calculation in the coordinate space within the region $[-400, 400]$ a.u. To avoid spurious reflections from the spatial boundaries, the electron wave function is multiplied by an absorbing boundary. We obtain the ionization probability of the atom by counting the absorbed wave function. The laser pulse is described by $F_0' f(t) sin(\omega' t)$. $f(t)$ is the trapezoidal envelop with 2 cycle rising and 2 cycle falling edges and 3 cycle plateau.

3. Result and discussion

Figure 2(a) shows the ionization of the atom as a function of laser intensity. The laser intensity changes from 530 to 850 TW/cm^2 and the wavelength is fixed at 550 nm. It is shown that the ionization peaks at specific intensities. These peaks are located at integer channels (the upper axis). We also show the total excitation probability (the sum over excitation probabilities of all eigenstates) of solids in Fig. 2(b). The intensity varies from 0.3 to 2.2 TW/cm^2 and the wavelength is fixed at 2200 nm. Compared with the laser intensity used in the experiment of ZnO bulk crystal [28], the intensity used in this paper will not damage the material. As shown in Fig. 2(b), the excitation probability also exhibits a strong intensity-dependent modulation. The interval of modulation is about 0.4 TW/cm^2.

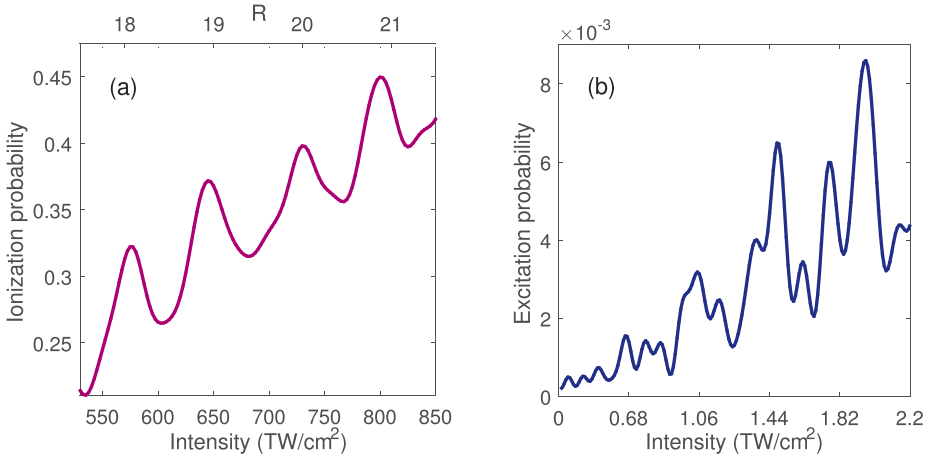

Fig. 2. (a) The ionization probability of the atom as a function of the laser intensity. The intensity varies from 530 TW/cm^2 to 850 TW/cm^2. The wavelength is fixed at 550 nm. (b) The sum over excitation probability of all eigenstates of solids. The intensity varies from 0.3 TW/cm^2 to 2.2 TW/cm^2 and the wavelength is fixed at 2200 nm.

To have a deeper insight into the intensity-dependent modulation, we select the eigenstate on the top of VB as the initial state to investigate the electronic excitation. The result is presented in Fig. 3(a). Similar to the atom, a series of resonance-like enhancements are produced at specific laser intensities. Moreover, some small oscillations appear among the enhancements and the number of oscillations between adjacent enhancements is constant. We also simulate the excitation probability driven by laser pulses with different intensities (0.01 TW/cm^2 $\leq I_0 \leq$ 2 TW/cm^2) and wavelengths (1500 nm $\leq \lambda \leq$ 2300 nm). The result is shown in Fig. 3(b). One can see that the excitation probability exhibit regular shaped ridges and the shaped ridges occur more frequently with the increase of intensity or wavelength. As the laser intensity decreases, the shaped ridges disappear gradually.

Optics EXPRESS

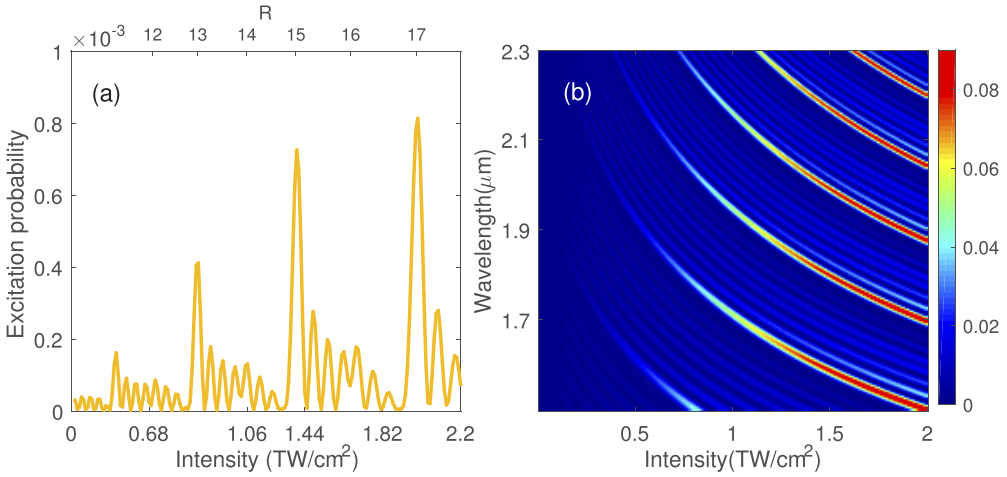

Fig. 3. The eigenstate on the top of VB is selected as the initial state. (a) The excitation probability of electrons driven by the laser plus with the intensity varies from 0.3 TW/cm^2 to 2.2 TW/cm^2 and the wavelength is fixed at 2200 nm. (b) The excitation probability driven by laser pulses with intensities from 0.01 to 2 TW/cm^2 and wavelengths from 1500 to 2300 nm.

3.1. Mechanism of electronic excitation in solids

To understand the underlying mechanism of the shaped ridges, we investigate the electronic excitation processes based on an ensemble of electronic trajectories in the reciprocal space. The trajectory ensemble is formed by the trajectories from different excitation times t_i and different initial crystal momentum k_0. In this case, the electron can be excited from the VB to the CB1 with certain probability. When the depletion of the initial state can be neglected, the complex amplitude of excitation rate can be written as [30,37]:

$$\chi(t_i) = e^{iS_{c,k_0}(t_i,t_0)}\Omega_{cv}(t_i)e^{-iS_{v,k_0}(t_i,t_0)}. \tag{9}$$

$S_{v,k_0}(t_i,t_0) = \int_{t_0}^{t_i} d\tau E_v(k(\tau))$ and $S_{c,k_0}(t_i,t_0) = \int_{t_0}^{t_i} d\tau E_c(k(\tau))$ are the phases gathered in VB and CB1, respectively. $\Omega_{cv}(t) = -id_{cv}(k(t))F(t)$ is Rabi frequency and $d_{cv}(k(t))$ denotes the transition matrix elements between VB and CB1, where $k(t) = k_0 + A(t)$ and $A(t)$ is the vector potential of the laser field. In our simulation, the eigenstate at the top of the VB is chosen as the initial state, which indicates $k_0 = 0$. This method fully includes quantum interference effects, thus the trajectories of different excitation times are coherent with each other.

Based on the trajectory ensemble, the interference among the electronic trajectories within different excitation times is investigated. The intensity of the interference is given by $\left|\int_t^{t'} d\tau\chi(\tau)\right|^2$, which represents the probability of electronic excitation. We first consider the trajectories excited in two adjacent optical cycles. The two cycles can be divided into τ_1, τ_2, τ_3 and τ_4, as shown in Fig. 4. τ_1 and τ_2 belong to the same cycle, and the interference of the trajectories within τ_1 and τ_2 is called intracycle interference. τ_1 and τ_3 belong to different cycles, and the interference of the trajectories within τ_1 and τ_3 is called intercycle interference. The intra- (the solids line) and intercycle interference (the dashed line) with wavelength from 1700 to 2500 nm are shown in Fig. 5(a), respectively. Laser intensity is fixed at 1.4 TW/cm^2. The peaks of intracycle interference appear at particular wavelengths 1830 nm, 2024 nm, etc. The peaks of the intercycle interference appear at 1830 nm, 1928 nm, 2024 nm, etc. One can see that the wavelength difference between two adjacent intercycle interference peaks is almost half of that for the

Optics EXPRESS

intracycle interference. We superimpose the complex amplitudes of the trajectories excited in τ_1, τ_2 and τ_3. The module (the dotted line) is shown in Fig. 5(a). It is shown that the peaks appear at the wavelength 1830 nm, 2024 nm, etc, where the intra- and intercycle interference reach a maximum. The secondary peaks occur at 1724 nm, 1928 nm, etc. At these wavelengths, the intracycle interference reaches a minimum and the intercycle interference reaches a maximum.

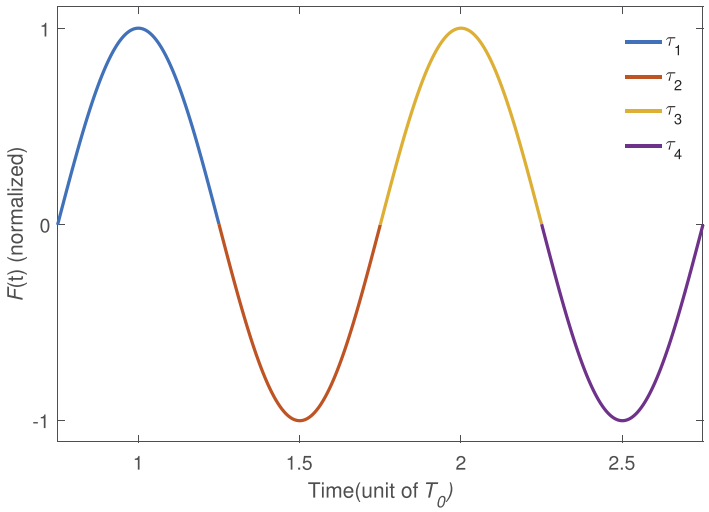

Fig. 4. The normalized electric field divided into τ_1, τ_2, τ_3 and τ_4.

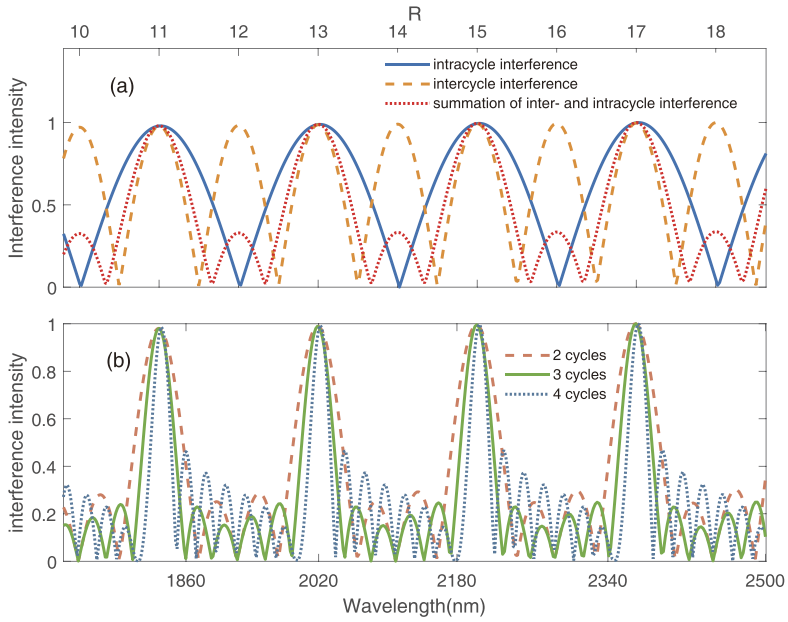

Fig. 5. The eigenstate on the top of VB is selected as the initial state. (a) The normalized intra- (the solids line) and intercycle interference (the dashed line) with the driving wavelength λ from 1700 to 2500 nm. Laser intensity is fixed at 1.4 TW/cm^2. The interference of the trajectories within τ_1, τ_2 and τ_3 (the dotted line) is also shown. (b) The normalized interference of the trajectories within 2, 3 and 4 cycles, respectively.

Optics EXPRESS

In order to simplify the analysis of intra- and intercycle interference, we consider several representative trajectories. Since the excitation probability is maximized when the electron passes near $k = 0$. When eigenstate $k_0 = 0$ is selected as the initial state, we select $t_1 = T_0$, $t_2 = \frac{3T_0}{2}$, $t_3 = 2T_0$ as the excitation times of the trajectories, respectively. The complex amplitudes are expressed as

$$\begin{aligned}\chi(t_1) &= \Omega_{cv}(t_1)e^{iS(t_1,t_0)},\\ \chi(t_2) &= \Omega_{cv}(t_2)e^{iS(t_2,t_0)},\\ \chi(t_3) &= \Omega_{cv}(t_3)e^{iS(t_3,t_0)},\end{aligned} \tag{10}$$

respectively, where $S(t,t_0) = \int_{t_0}^{t}(E_c(k(\tau) - E_v(k(\tau))d\tau$ is the classical action and $\Omega_{cv}(t_1) = -\Omega_{cv}(t_2) = \Omega_{cv}(t_3)$. For the intracycle interference, we superpose $\chi(t_1)$ and $\chi(t_2)$ and get the expression

$$\chi' = \Omega_{cv}(t_1)e^{iS(t_1,t_0)}(1 - e^{iS(t_2,t_1)}). \tag{11}$$

χ' reaches a maximum with the condition $S(t_2,t_1) = (2N-1)\pi$, where N is an integer. This condition can be further expressed by a average classical action $\overline{S} = \frac{1}{t_2-t_1}\int_{t_1}^{t_2}(E_c(k(\tau)-E_v(k(\tau))d\tau$:

$$(t_2 - t_1)\frac{2\overline{S}}{T_0} = (2N-1)\omega. \tag{12}$$

Analogous to the cases in the atom, we define the channel-closing number in solids

$$R = \frac{\overline{S}}{\omega}. \tag{13}$$

According to Eq. (11) and Eq. (12), the intracycle interference will reach a maximum when $R = \frac{T_0}{2(t_2-t_1)}(2N-1)$, here is $(2N-1)$. This can be observed in Fig. 5(a) with the coordinate R on the top. Note that only a small proportion of electrons near $k = 0$ on VB can tunnel into CBs. In this case, the coefficient $\frac{T_0}{2(t_2-t_1)}$ is approximately equal to 1. Following the same derivation, the intercycle interference can be obtained by superposing $\chi(t_1)$ and $\chi(t_3)$, and the expression is

$$\chi'' = \Omega_{cv}(t_1)e^{iS(t_1,t_0)}(1 + e^{iS(t_3,t_1)}). \tag{14}$$

When $\overline{S} = \frac{1}{t_3-t_1}\int_{t_1}^{t_3}(E_c(k(\tau) - E_v(k(\tau))d\tau = N\omega$, i.e., R is integer, the intercycle interference reaches a maximum. This can be observed by the correspondence between R and the intercycle interference as shown in Fig. 5(a).

Then we discuss about the small oscillations of the excitation probability. Figure 5(b) shows interference of the electronic trajectories within 2, 3 and 4 cycles, respectively. One can see that the number of the oscillations between adjacent enhancements changes from 2 to 6 with the increase of optical cycle. When one more optical cycle is involved, two more small oscillations appear. This is similar to that of multiple slit interference.

The excitation of the eigenstates from $k_0 = -0.1214$ to 0 and corresponding values of R are shown in Fig. 6. Note that excitation of the eigenstates from $k_0 = 0$ to 0.1214 is symmetric with the result shown in Fig. 6. The driving wavelength λ varies from 1700 to 2500 nm and the laser intensity is fixed at 1.4 TW/cm^2. It is shown that the enhancements of excitation occur at specific eigenstates and wavelengths. The dotted and dashed lines represent the integer and odd channels of inter- and intracycle interference, respectively. One can see that the two channels will shift as the eigenstate changes. When the dotted line intersects the dashed line, i.e, R is odd for intracycle interference and an integer for intercycle interference, the excitation will exhibit enhancements.

The above results and analysis show that the electronic excitation in solids is very different from that in the atom. This difference is attributed to the band structure of solids system. In

Optics EXPRESS

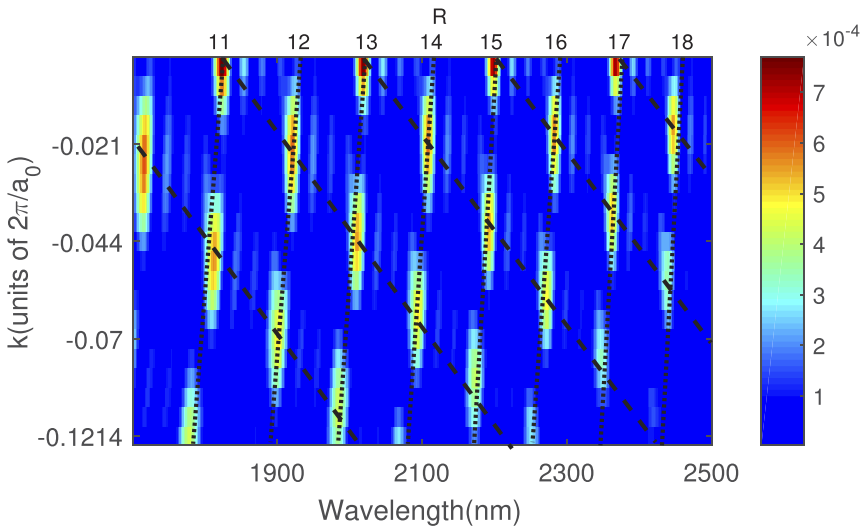

Fig. 6. The electronic excitation of the eigenstates that from $k_0 = -0.121$ to 0. The driving wavelength λ varies from 1700 to 2500 nm and the laser intensity is fixed at 1.4 TW/cm^2. The dotted lines represent the integer channel closing numbers of intercycle interference from 11 to 18. The dashed lines represent the odd channel closing numbers of intracycle interference from 9 to 17.

solids, the electrons excited at different moments have the same finial momentum when the laser pulse is over. Therefore, intra- and intercycle interference can happen among the electronic trajectories. As we discussed above, the excitation probability exhibits enhancements when R is odd for intracycle interference and an integer for intercycle interference. In the atom, irradiated by laser field, the electrons are localized in the ground state and have opportunities to tunnel to continue. The electrons that are ionized with half-cycle-time interval, e.g., ionization at $t = T_0$ and $\frac{3T_0}{2}$ (shown in Fig. 4), experience reversed electric field. Thus the momentums of the electrons are opposite. The electronic trajectories do not interfere with each other. However, for the electrons ionized with one-cycle-time interval, e.g., ionization at $t = T_0$ and $2T_0$, the momentums of the electrons are the same. The electronic trajectories can interfere with each other. As a result, the ionization probability of the atom peaks in integer channels.

3.2. *Observation of the channel-closing effect in solids*

We next consider how to observe the channel-closing effects in solids. One possible method is using the photoemission spectroscopy. Here we propose an all-optical method based on the HHG in solids. Figure 7 shows the harmonic yield and the corresponding excitation probability as a function of R, respectively. The initial state is the eigenstate on the top of VB. Same as the excitation probability, one can see that the harmonic yield is also drastically enhanced in the odd channels. It indicates that the harmonic yield and the excitation probability have a strong relevance and it is feasible to observe the channel-closing effects by detecting HHG in solids. We also simulate the excitation probability and the harmonic yield when all the eigenstates on VB are selected as the initial state. The result shows that the harmonic yield and the excitation probability also have a relevance.

Figure 8 shows the harmonic spectra with $R = 14.6$, 15 and 15.8 , respective. The eigenstate on the top of VB is selected as the initial state. The plateau (from 5 to 19 orders) of the harmonic spectrum typically originates from the transition of the electron from CB1 to VB. It is shown that the harmonic intensity is enhanced throughout the plateau in odd channels. In contrast,

Optics EXPRESS

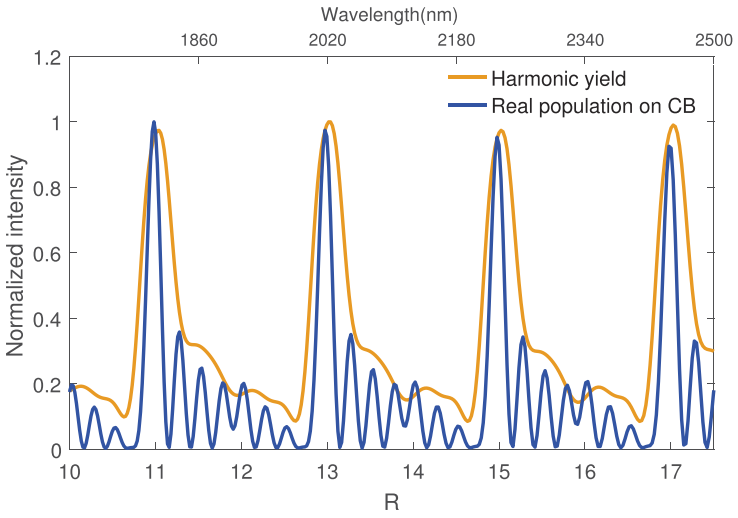

Fig. 7. The normalized harmonic yield and the real population on CB1 with R from 9.8 to 18.6. The eigenstate on the top of VB is selected as the initial state. The wavelength changes from 1700 nm to 2500 nm and the intensity is fixed at 1.4 TW/cm^2.

the enhancement of HHG in the atom only occurs in a portion of the plateau. When solids are irradiated by a laser pulse, electrons in VB have opportunities to excite into CB1. The exciting electrons are not fixed at the crystal momentum where they are excited. The Bloch electrons will be accelerated with the laser field following $\hbar dk/dt = -eF$, and can move a wide range of k. As a result, the electrons can transit back from CB1 to VB at different k, emitting photons with energy covering the whole plateau regions. This explains why the channel-closing effects contribute to the enhancement throughout the plateau region in solids.

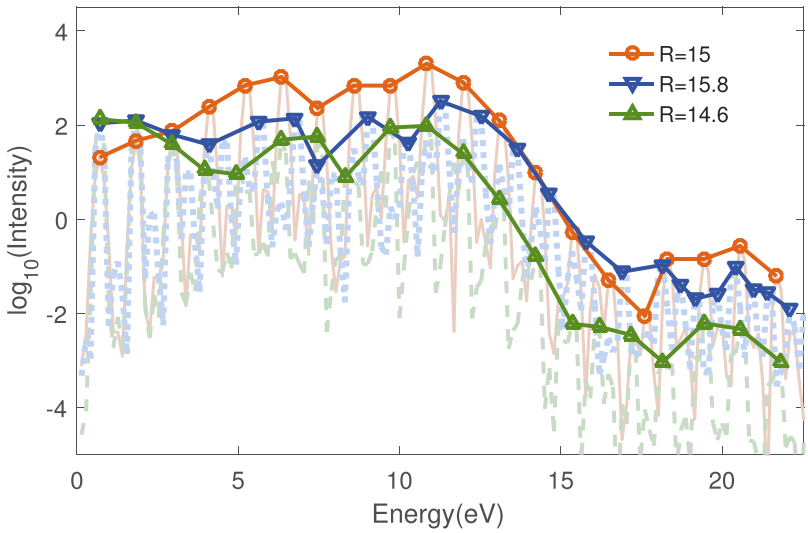

Fig. 8. The harmonic spectra with R = 14.6 (upward-pointing triangles), 15 (circles) and 15.8 (downward-pointing triangles). The eigenstate on the top of VB is selected as the initial state.

Optics EXPRESS

4. Conclusion

We investigate the electronic excitation in solids by solving TDSE in length gauge. With the initial state filling CB, the excitation probability exhibits obvious intensity dependent modulation. We also select an eigenstate as the initial state. The excitation probability exhibits intense intensity and wavelength dependences demonstrating resonance-like enhancements and small oscillations. These phenomena are explained by the interference of the electronic trajectories with different excitation times. We further relate the modulation to the channel-closing effects in solids. The results show that the enhancements only occur when the value of channel is odd for intracycle interference and an integer for intercycle interference, which is different from that in the atom. We also confirm that the channel-closing effects can be detected by solid HHG.

Funding

National Key R&D Program (2017YFE0116600); National Natural Science Foundation of China (91950202, 11627809, 11874165, 11704137, 11774109); Science and Technology Planning Project of Guangdong Province (2018B090944001).

Acknowledgments

Numerical simulations presented in this paper were carried out using the High Performance Computing Center experimental testbed in SCTS/CGCL (see http://grid.hust.edu.cn/hpcc).

Disclosures

The authors declare no conflicts of interest

References

1. P. Agostini, F. Fabre, G. Mainfray, G. Petite, and N. K. Rahman, "Free-free transitions following six-photon ionization of xenon atoms," Phys. Rev. Lett. **42**(17), 1127–1130 (1979).
2. M. Ferray, A. L'Huillier, X. F. Li, L. A. Lompre, G. Mainfray, and C. Manus, "Multiple-harmonic conversion of 1064 nm radiation in rare gases," J. Phys. B **21**(3), L31–L35 (1988).
3. A. McPherson, G. Gibson, H. Jara, U. Johann, T. S. Luk, I. A. McIntyre, K. Boyer, and C. K. Rhodes, "Studies of multiphoton production of vacuum-ultraviolet radiation in the rare gases," J. Opt. Soc. Am. B **4**(4), 595–601 (1987).
4. A. l'Huillier, L. A. Lompre, G. Mainfray, and C. Manus, "Multiply charged ions induced by multiphoton absorption in rare gases at 0.53 μm," Phys. Rev. A **27**(5), 2503–2512 (1983).
5. S. Augst, D. Strickland, D. D. Meyerhofer, S. L. Chin, and J. H. Eberly, "Tunneling ionization of noble gases in a high-intensity laser field," Phys. Rev. Lett. **63**(20), 2212–2215 (1989).
6. J. Javanainen, J. H. Eberly, and Q. Su, "Numerical simulations of multiphoton ionization and above-threshold electron spectra," Phys. Rev. A **38**(7), 3430–3446 (1988).
7. G. G. Paulus, W. Becker, W. Nicklich, and H. Walther, "Rescattering effects in above-threshold ionization: a classical model," J. Phys. B **27**(21), L703–L708 (1994).
8. M. Lewenstein, K. C. Kulander, K. J. Schafer, and P. H. Bucksbaum, "Rings in above-threshold ionization: A quasiclassical analysis," Phys. Rev. A **51**(2), 1495–1507 (1995).
9. F. Krausz and M. Ivanov, "Attosecond physics," Rev. Mod. Phys. **81**(1), 163–234 (2009).
10. J. G. Story, D. I. Duncan, and T. F. Gallagher, "Channel closing in multiphoton ionization of mg," Phys. Rev. A **49**(5), 3875–3880 (1994).
11. J. Itatani, J. Levesque, D. Zeidler, H. Niikura, H. Pépin, J. C. Kieffer, P. B. Corkum, and D. M. Villeneuve, "Tomographic imaging of molecular orbitals," Nature **432**(7019), 867–871 (2004).
12. X. Zhu, M. Qin, Q. Zhang, Y. Li, Z. Xu, and P. Lu, "Influence of large permanent dipoles on molecular orbital tomography," Opt. Express **21**(5), 5255–5268 (2013).
13. B. Wang, L. He, Y. He, Y. Zhang, R. Shao, P. Lan, and P. Lu, "All-optical measurement of high-order fractional molecular echoes by high-order harmonic generation," Opt. Express **27**(21), 30172–30181 (2019).
14. X. Huang, Q. Zhang, S. Xu, X. Fu, X. Han, W. Cao, and P. Lu, "Coulomb focusing in retrapped ionization with near-circularly polarized laser field," arXiv:1911.09805 (2019); to be published *in* Opt. Express.
15. Y. Feng, M. Li, S. Luo, K. Liu, B. Du, Y. Zhou, and P. Lu, "Semiclassical analysis of photoelectron interference in a synthesized two-color laser pulse," arXiv:1911.04035 (2019).
16. N. Teeny, E. Yakaboylu, H. Bauke, and C. H. Keitel, "Ionization time and exit momentum in strong-field tunnel ionization," Phys. Rev. Lett. **116**(6), 063003 (2016).

Optics EXPRESS

17. S. Luo, M. Li, W. Xie, K. Liu, Y. Feng, B. Du, Y. Zhou, and P. Lu, "Exit momentum and instantaneous ionization rate of nonadiabatic tunneling ionization in elliptically polarized laser fields," Phys. Rev. A **99**(5), 053422 (2019).
18. Y. Zhao, Y. Zhou, J. Liang, Z. Zeng, Q. Ke, Y. Liu, M. Li, and P. Lu, "Frustrated tunneling ionization in the elliptically polarized strong laser fields," Opt. Express **27**(15), 21689–21700 (2019).
19. P. H. Bucksbaum, A. Sanpera, and M. Lewenstein, "Resonant double-excitation induced by wiggling ATI electrons," J. Phys. B **30**(23), L843–L850 (1997).
20. P. Hansch, M. A. Walker, and L. D. Van Woerkom, "Resonant hot-electron production in above-threshold ionization," Phys. Rev. A **55**(4), R2535–R2538 (1997).
21. M. J. Nandor, M. A. Walker, L. D. Van Woerkom, and H. G. Muller, "Detailed comparison of above-threshold-ionization spectra from accurate numerical integrations and high-resolution measurements," Phys. Rev. A **60**(3), R1771–R1774 (1999).
22. E. S. Toma, P. Antoine, A. de Bohan, and H. G. Muller, "Resonance-enhanced high-harmonic generation," J. Phys. B **32**(24), 5843–5852 (1999).
23. S. V. Popruzhenko, P. A. Korneev, S. P. Goreslavski, and W. Becker, "Laser-induced recollision phenomena: Interference resonances at channel closings," Phys. Rev. Lett. **89**(2), 023001 (2002).
24. G. G. Paulus, F. Grasbon, H. Walther, R. Kopold, and W. Becker, "Channel-closing-induced resonances in the above-threshold ionization plateau," Phys. Rev. A **64**(2), 021401 (2001).
25. R. Kopold, W. Becker, M. Kleber, and G. G. Paulus, "Channel-closing effects in high-order above-threshold ionization and high-order harmonic generation," J. Phys. B **35**(2), 217–232 (2002).
26. A. Schiffrin, T. Paasch-Colberg, N. Karpowicz, V. Apalkov, D. Gerster, S. Muhlbrandt, M. Korbman, J. Reichert, M. Schultze, S. Holzner, J. V. Barth, R. Kienberger, R. Ernstorfer, V. S. Yakovlev, M. I. Stockman, and F. Krausz, "Optical-field-induced current in dielectrics," Nature **493**(7430), 70–74 (2013).
27. D. N. Basov, R. D. Averitt, and D. Hsieh, "Towards properties on demand in quantum materials," Nat. Mater. **16**(11), 1077–1088 (2017).
28. S. Ghimire, A. D. DiChiara, E. Sistrunk, P. Agostini, L. F. DiMauro, and D. A. Reis, "Observation of high-order harmonic generation in a bulk crystal," Nat. Phys. **7**(2), 138–141 (2011).
29. T. T. Luu, M. Garg, S. Y. Kruchinin, A. Moulet, M. T. Hassan, and E. Goulielmakis, "Extreme ultraviolet high-harmonic spectroscopy of solids," Nature **521**(7553), 498–502 (2015).
30. L. Li, P. Lan, X. Zhu, T. Huang, Q. Zhang, M. Lein, and P. Lu, "Reciprocal-space-trajectory perspective on high-harmonic generation in solids," Phys. Rev. Lett. **122**(19), 193901 (2019).
31. S. Jiang, J. Chen, H. Wei, C. Yu, R. Lu, and C. D. Lin, "Role of the transition dipole amplitude and phase on the generation of odd and even high-order harmonics in crystals," Phys. Rev. Lett. **120**(25), 253201 (2018).
32. C. Yu, X. Zhang, S. Jiang, X. Cao, G. Yuan, T. Wu, L. Bai, and R. Lu, "Dependence of high-order-harmonic generation on dipole moment in Sio_2 crystals," Phys. Rev. A **94**(1), 013846 (2016).
33. W. Li, C. Qin, T. Han, H. Chen, B. Wang, and P. Lu, "Bloch oscillations in photonic spectral lattices through phase-mismatched four-wave mixing," Opt. Lett. **44**(22), 5430–5433 (2019).
34. C. Yu, S. Jiang, T. Wu, G. Yuan, Z. Wang, C. Jin, and R. Lu, "Two-dimensional imaging of energy bands from crystal orientation dependent higher-order harmonic spectra in h – BN," Phys. Rev. B **98**(8), 085439 (2018).
35. L. Li, P. Lan, L. He, W. Cao, Q. Zhang, and P. Lu, "Determination of electron band structure using temporal interferometry," arXiv:1908.07283 (2019).
36. T.-Y. Du, D. Tang, and X.-B. Bian, "Subcycle interference in high-order harmonic generation from solids," Phys. Rev. A **98**(6), 063416 (2018).
37. G. Vampa, C. R. McDonald, G. Orlando, P. B. Corkum, and T. Brabec, "Semiclassical analysis of high harmonic generation in bulk crystals," Phys. Rev. B **91**(6), 064302 (2015).
38. W.-J. Wei, X.-X. Jiang, L.-Y. Dong, W.-W. Liu, X.-B. Han, Y. Qin, K. Li, W. Li, Z.-S. Lin, X.-H. Bu, and P.-X. Lu, "Regulating second-harmonic generation by van der waals interactions in two-dimensional lead halide perovskite nanosheets," J. Am. Chem. Soc. **141**(23), 9134–9139 (2019). PMID: 31131600.
39. V. E. Gruzdev, "Photoionization rate in wide band-gap crystals," Phys. Rev. B **75**(20), 205106 (2007).
40. V. Gruzdev and O. Sergaeva, "Ultrafast modification of band structure of wide-band-gap solids by ultrashort pulses of laser-driven electron oscillations," Phys. Rev. B **98**(11), 115202 (2018).
41. P. A. Zhokhov and A. M. Zheltikov, "Field-cycle-resolved photoionization in solids," Phys. Rev. Lett. **113**(13), 133903 (2014).
42. C. R. McDonald, G. Vampa, P. B. Corkum, and T. Brabec, "Intense-laser solid state physics: Unraveling the difference between semiconductors and dielectrics," Phys. Rev. Lett. **118**(17), 173601 (2017).
43. H. Mashiko, K. Oguri, T. Yamaguchi, A. Suda, and H. Gotoh, "Petahertz optical drive with wide-bandgap semiconductor," Nat. Phys. **12**(8), 741–745 (2016).
44. F. Krausz and M. I. Stockman, "Attosecond metrology: from electron capture to future signal processing," Nat. Photonics **8**(3), 205–213 (2014).
45. M. Sivis, M. Taucer, G. Vampa, K. Johnston, A. Staudte, A. Y. Naumov, D. M. Villeneuve, C. Ropers, and P. B. Corkum, "Tailored semiconductors for high-harmonic optoelectronics," Science **357**(6348), 303–306 (2017).
46. A. Schiffrin, T. Paasch-Colberg, N. Karpowicz, V. Apalkov, D. Gerster, S. Muhlbrandt, M. Korbman, J. Reichert, M. Schultze, S. Holzner, J. V. Barth, R. Kienberger, R. Ernstorfer, V. S. Yakovlev, M. I. Stockman, and F. Krausz, "Optical-field-induced current in dielectrics," Nature **493**(7430), 70–74 (2013).

Optics EXPRESS

47. N. E. Christensen and I. Gorczyca, "Optical and structural properties of iii-v nitrides under pressure," Phys. Rev. B **50**(7), 4397–4415 (1994).
48. P. G. Hawkins, M. Y. Ivanov, and V. S. Yakovlev, "Effect of multiple conduction bands on high-harmonic emission from dielectrics," Phys. Rev. A **91**(1), 013405 (2015).
49. X. Li, W. Liu, Y. Song, C. Zhang, H. Long, K. Wang, B. Wang, and P. Lu, "Enhancement of the second harmonic generation from ws 2 monolayers by cooperating with dielectric microspheres," Adv. Opt. Mater. **7**(3), 1801270 (2019).
50. D. M. Kinyua, H. Long, X. Xing, S. Njoroge, K. Wang, B. Wang, and P. Lu, "Gigahertz acoustic vibrations of ga-doped ZnO nanoparticle array," Nanotechnology **30**(30), 305201 (2019).
51. J. C. Slater, "A soluble problem in energy bands," Phys. Rev. **87**(5), 807–835 (1952).
52. B. M. Breid, D. Witthaut, and H. J. Korsch, "Bloch–zener oscillations," New J. Phys. **8**(7), 110 (2006).
53. R. Chang, S. Potnis, R. Ramos, C. Zhuang, M. Hallaji, A. Hayat, F. Duque-Gomez, J. E. Sipe, and A. M. Steinberg, "Observing the onset of effective mass," Phys. Rev. Lett. **112**(17), 170404 (2014).
54. J. Li, Q. Zhang, L. Li, X. Zhu, T. Huang, P. Lan, and P. Lu, "Orientation dependence of high-order harmonic generation in nanowire," Phys. Rev. A **99**(3), 033421 (2019).
55. M. Wu, D. A. Browne, K. J. Schafer, and M. B. Gaarde, "Multilevel perspective on high-order harmonic generation in solids," Phys. Rev. A **94**(6), 063403 (2016).
56. T.-Y. Du and X.-B. Bian, "Quasi-classical analysis of the dynamics of the high-order harmonic generation from solids," Opt. Express **25**(1), 151–158 (2017).
57. M. Wu, S. Ghimire, D. A. Reis, K. J. Schafer, and M. B. Gaarde, "High-harmonic generation from bloch electrons in solids," Phys. Rev. A **91**(4), 043839 (2015).
58. Z. Guan, X.-X. Zhou, and X.-B. Bian, "High-order-harmonic generation from periodic potentials driven by few-cycle laser pulses," Phys. Rev. A **93**(3), 033852 (2016).
59. X. Liu, X. Zhu, P. Lan, X. Zhang, D. Wang, Q. Zhang, and P. Lu, "Time-dependent population imaging for high-order-harmonic generation in solids," Phys. Rev. A **95**(6), 063419 (2017).
60. M. D. Feit, J. A. Fleck, and A. Steiger, "Solution of the schrödinger equation by a spectral method," J. Comput. Phys. **47**(3), 412–433 (1982).